

pubs.acs.org/JPCC Article

Development and Applications of ReaxFF Reactive Force Fields for Group-III Gas-Phase Precursors and Surface Reactions with Graphene in Metal—Organic Chemical Vapor Deposition Synthesis

Siavash Rajabpour, Qian Mao, Nadire Nayir, Joshua A. Robinson, and Adri C. T. van Duin*



Cite This: J. Phys. Chem. C 2021, 125, 10747–10758



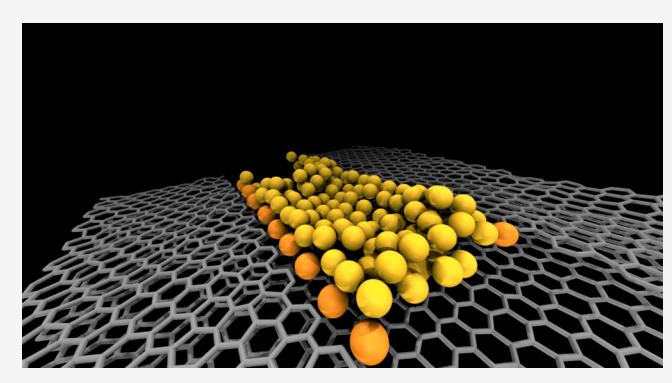
ACCESS

III Metrics & More



Supporting Information

ABSTRACT: Two-dimensional (2D) materials exhibit a wide range of optical, electronic, and quantum properties divergent from their bulk counterparts. To realize scalable 2D materials, metal—organic chemical vapor deposition (MOCVD) is often used. Here, we report two ReaxFF reactive force fields, GaCH-2020 and InCH-2020, which were developed to investigate the MOCVD gas-phase reactions of Ga and In film growth from trimethylgallium (TMGa) and trimethylindium (TMIn) precursors, respectively, and the surface interactions of TMGa and TMIn with graphene. The newly developed force fields were applied to determine the optimal conditions for the thermal decomposition of TMGa/TMIn to achieve Ga/In nanoclusters with low impurities. Additionally, the cluster formation of Ga/In on a graphene substrate with different



vacancies and edges was studied. It was found that a graphene with Ga-functionalized monovacancies could help conduct directional Ga cluster growth via covalent bonds. Moreover, under specific growth conditions, we found that Ga atoms growing on armchairedged graphene not only exhibited a superior growth ratio to In atoms but also produced a widely spread 2D thin layer between graphene edges.

1. INTRODUCTION

The heteroepitaxial growth of group-III nitride semiconductors has been integrated into a wide range of optoelectronic devices such as laser diodes, light-emitting diodes, Group-III nitride films are usually grown heteroepitaxially on foreign substrates such as silicon, sapphire, and silicon carbide due to the complex production and high cost of native substrates. However, large differences in thermal expansion coefficients and lattice parameter mismatch between the epilayer and substrate lead to stress and high defect density in films. These defects act as current leakage pathways, charge carrier scatters, and nonradiative recombination sites, thus deteriorating the device performance. To mitigate the lattice and thermal mismatch, thereby enhancing the crystal quality of an epitaxial layer, a thin buffer layer of AlN or GaN is generally grown prior to the growth of films.

Van der Waals epitaxy offers a new approach to direct heteroepitaxy where thermal expansion coefficients and lattice parameters of the epilayer and substrate are notably different. This process has been employed to achieve heteroepitaxial growth of inorganic and organic 16,17 material systems as well as two-dimensional (2D) heterostructures. The van der Waals epitaxial growth on 2D layered materials exploits the lack of surface dangling bonds of 2D layered materials, where

the growing epilayer interacts with weak van der Waals forces instead of the covalent/metallic bonds in direct heteroepitaxy. As a result, there is a growing interest in implementing 2D layered materials as a substrate for group-III nitride growth to minimize the strain at the interface. ^{20–23} It should be noted that the growth of a three-dimensional (3D) epilayer on a 2D substrate is known as quasi van der Waals epitaxy, ^{24,25} where the epilayer interaction with the substrate might not be purely van der Waals due to the covalent bonding of group-III nitrides.

Graphene, a single layer of sp² carbon, is an attractive candidate as a substrate because of the van der Waals interactions with its environment and the hexagonal arrangement of atoms in graphene, which is similar to the (0001) *c*-plane of group-III nitrides. Furthermore, the thermal stability, high decomposition temperature, transferability, optical transparency, and electrical conductivity make graphene a promising substrate for group-III nitride nanowires^{26–28} and

Received: March 4, 2021 Revised: April 21, 2021 Published: May 6, 2021





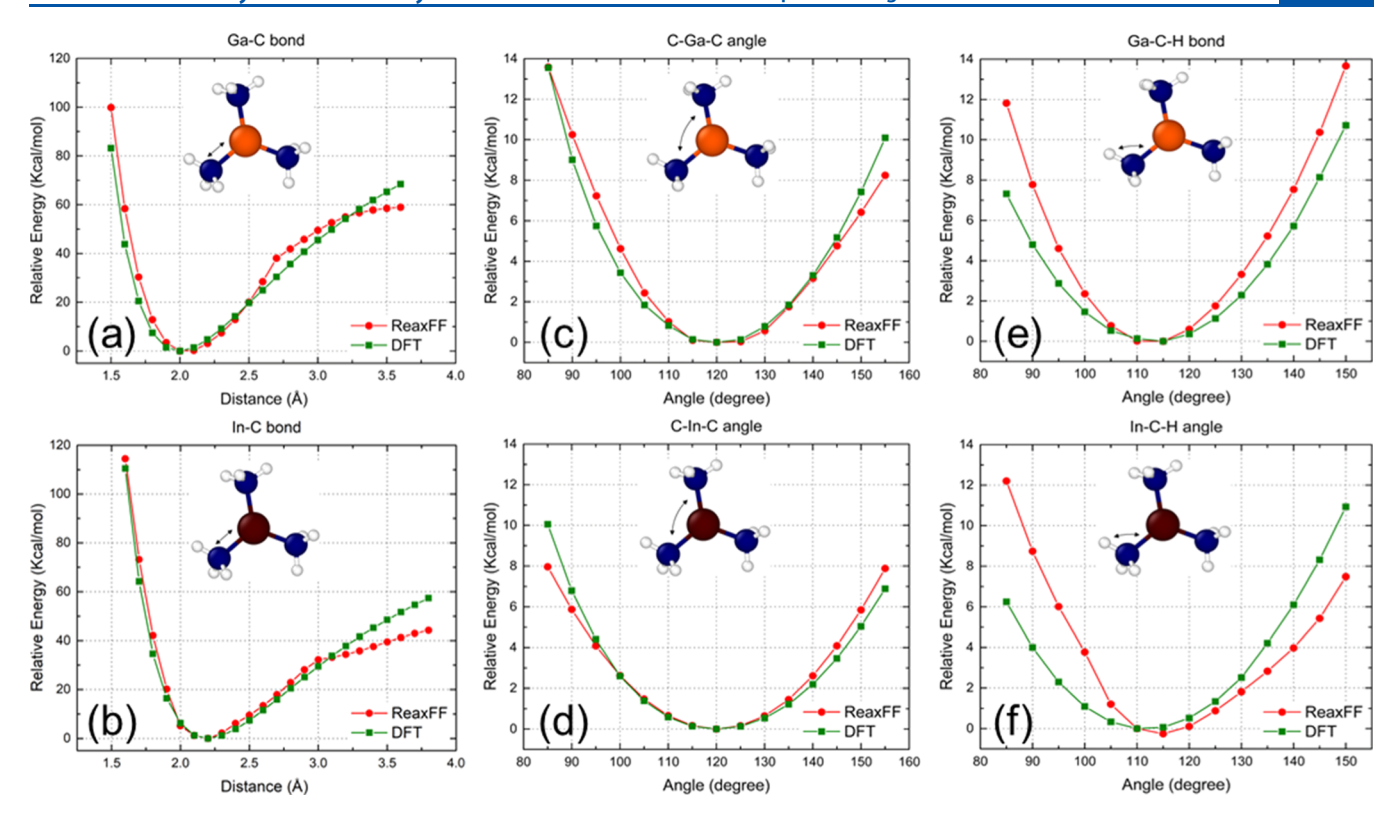


Figure 1. Comparison of DFT and ReaxFF bond dissociation energies for (a) Ga-C bond in TMGa and (b) In-C bond in TMIn. DFT and ReaxFF comparison of valence angle distortion energies for (c) C-Ga-C angle and (e) Ga-C-H angle in TMGa and (d) C-In-C angle and (f) In-C-H angle in TMIn. The small divergence in bond extension energies compared to DFT values is a result of lower optimization weights in the forcefield development methodology.

thin films. 20-23 For instance, Al Balushi et al. 29 demonstrated that the chemical reactivity and the thickness of a graphene substrate impact the nucleation of group-III nitride layers, and nitrogen defects affect the nucleation and growth of GaN and AlN on graphene. Qi et al.²¹ also reported the use of graphene as a buffer layer for the growth of AlN on a sapphire substrate, where the graphene reduces the AlN nuclei density while increasing the growth rate of individual grains. Sankaranarayanan et al.30 synthesized the hexagonal crystal structure of GaN on an N-doped monolayer graphene using the chemical vapor deposition technique. Spectroscopic measurements revealed no surface- and interface-related inhomogeneity in the GaN samples, thus enabling GaN to have high electron contents for attaining extraordinary device performance. However, despite extensive experimental studies, the underlying growth mechanism of group-III nitrides on graphene is not well understood. Computationally, Sangiovanni et al.³¹ used density functional theory (DFT) ab initio molecular dynamics (MD) with van der Waals corrections to identify atomistic pathways and the associated electronic mechanisms driving precursor and surface reactions during metal-organic vapor-phase epitaxy at elevated temperatures of AlN on graphene. Zhao et al.³² proposed a two-stage mechanism for plating Al on a graphene surface, of which the enthalpy, entropy, and Gibbs free energy were calculated, indicating that the first stage of the preparation of $(C_2H_5)_3Al$ and the second stage of decomposing (C₂H₅)₃Al and plating Al were both endothermic reactions. Because DFT methods can only treat relatively small systems—typically significantly smaller than 1000 atoms—these DFT studies could not well address the growth mechanisms of group-III nitrides on graphene, which

have raised the need for a more computationally effective computational tool that enables large-scale and long-time scale MD simulations of group-III nitrides.

In this work, we develop two ReaxFF reactive force fields (GaCH-2020 and InCH-2020) to investigate the metalorganic chemical vapor deposition (MOCVD) gas-phase reactions of Ga and In growth from TMGa and TMIn and their interactions with pristine and defective graphene substrates. In the application, we optimize the processing conditions during the thermal decomposition of TMGa/TMIn to minimize the impurities in Ga/In clusters. Furthermore, we demonstrate the possibility of utilizing a defective graphene for directional cluster growth. In addition, we aim to predict the parameters that are responsible for the 2D thin-layer growth of a Ga/In cluster by applying bilayer graphene with zigzag and armchair edges as a substrate under different growth conditions. For now, this investigation is limited to the interaction of group-III elements with graphene, but these force fields can also be implemented to understand the growth mechanism of group-III nitrides by the addition of nitrogen and more complex defects in graphene.

2. COMPUTATIONAL METHODS

2.1. ReaxFF Reactive Force Field. The ReaxFF reactive force field developed by van Duin et al.³³ is a bond-order-dependent interatomic potential that bridges the gap between quantum mechanical (QM) and classical MD methods by providing the capability of simulating large and chemically reactive systems. ReaxFF enables simulating bond formation/breakage over the course of MD simulations by updating the interatomic distances at every iteration, which is not possible

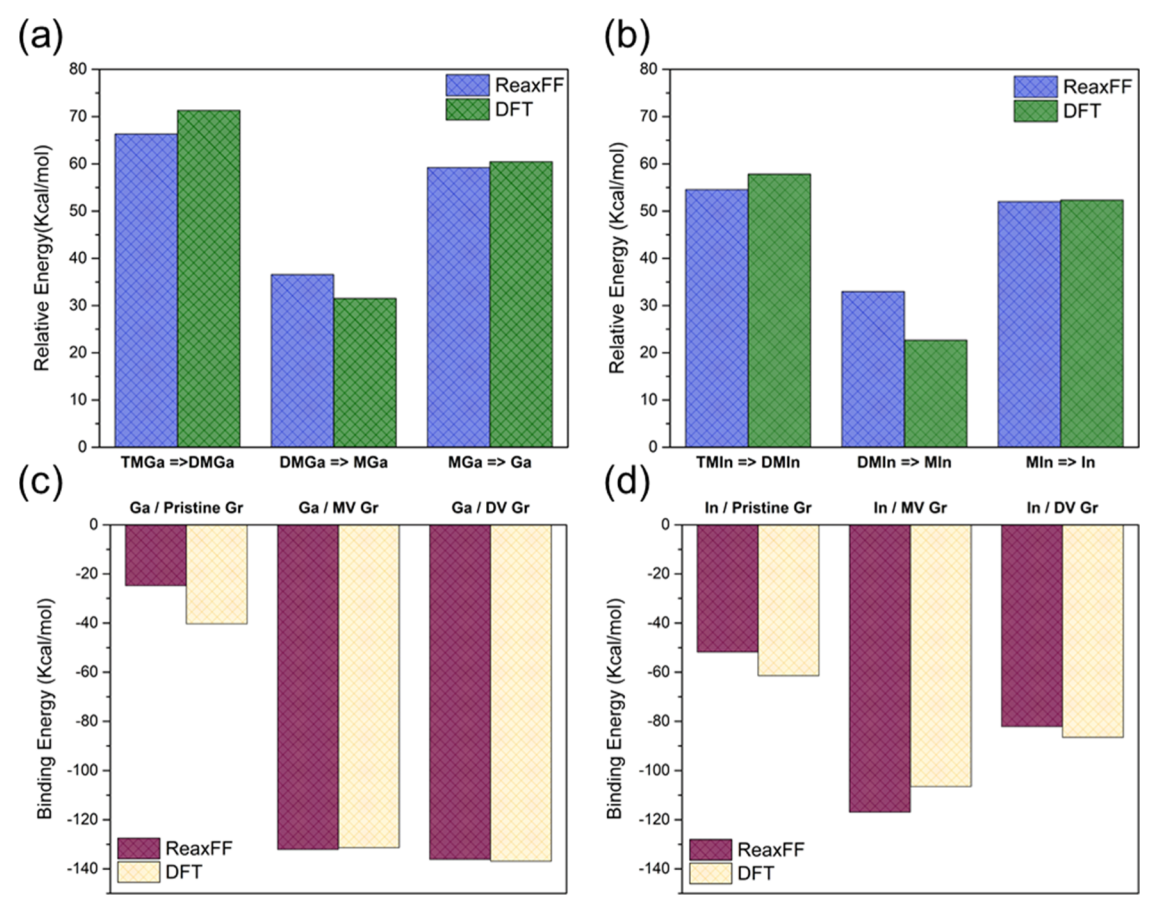


Figure 2. DFT and ReaxFF comparisons of dissociation energies of methyl from (a) TMGa, DMGa, and MGa, (b) TMIn, DMIn, and MIn. DFT and ReaxFF comparisons of adsorption energies of (c) Ga atom and (d) In atom on pristine graphene (pristine-Gr), and graphene with a monovacancy (MV-Gr) and a divacancy (DV-Gr).

by classical, non-reactive empirical force fields and is computationally too expensive to study by QM methods. ReaxFF force field parameters are obtained mainly by training against the QM structures and energies derived by methods such as DFT. 33,34 In ReaxFF force fields, the total energy of a system, E_{system} , is defined as

$$\begin{split} E_{\rm system} &= E_{\rm bond} + E_{\rm val} + E_{\rm tor} + E_{\rm vdWaals} + E_{\rm Coulomb} + E_{\rm lp} \\ &+ E_{\rm over} + E_{\rm under} \end{split} \tag{1}$$

where $E_{\rm bond}$, $E_{\rm val}$, $E_{\rm tor}$, $E_{\rm vdWaals}$, $E_{\rm Coulomb}$, $E_{\rm lp}$, $E_{\rm over}$, and $E_{\rm under}$ represent bond energy, valance energy, torsion angle energy, van der Waals energy, Coulomb energy, lone-pair energy, over-coordinate energy penalty, and under-coordination stability, respectively. ReaxFF MD simulations have been utilized to study reactive processes in thin-film growth, 35,36 semiconducting materials, 37,38 2D materials, $^{39-43}$ graphene, and other carbon-based materials.

2.2. Force Field Parameterization. GaCH-2020 and InCH-2020 potential parameters were trained against DFT data on periodic and non-periodic systems using a single-parameter parabolic method with a focus on TMGa and TMIn chemistries as the main gas precursors for Ga and In in MOCVD systems. Non-periodic DFT calculations were carried out using Jaguar⁵⁰ with the B3LYP functional and the PVDZ++ basis set. DFT calculations on periodic systems were carried out using the Quantum Espresso package⁵¹ in conjunction with projected augmented wave pseudopotentials^{52,53} and the

Perdew–Burke–Ernzerhof parametrization of the generalized gradient approximation exchange–correlation functional (GGA-PBE). A 5 × 5 × 1 Γ -centered k-point mesh was used to sample the Brillouin zone. Energy cut-offs for wavefunctions and charge densities were set to 408 and 4.080 eV, respectively, with a vacuum region of 20 Å along the out-of-plane direction in order to reduce the interactions between the replicas. The relaxation scheme of Broyden–Fletcher–Goldfarb–Shanno was employed with a force threshold of 0.025 eV Å $^{-1}$. The Marzari–Vanderbilt cold smearing scheme 55 was applied with a broadening of 0.1 eV.

The QM-based training set contains the Ga–C/In–C and Ga–H/In–H bond dissociation energies and C–Ga–C/C–In–C, Ga–C–H/In–C–H, H–Ga–H/H–In–H, C–C–Ga/C–C–In, H–Ga–C/H–In–C, and Ga–C–Ga/In–C–In valence angle distortion energies in $\text{Ga}(\text{CH}_3)_x/\text{In}(\text{CH}_3)_x$ (x=1,2, and 3) and other small molecules (Figures S1–S12). Moreover, the dissociation energies for the major reactions of the TMGa and TMIn decomposition into such as dimethylgallium (DMGa)/dimethylindium (DMIn) and methylgallium (MGa)/methylindium (MIn) in eqs 2–4 were added to the force fields' training data set.

$$TMGa/TMIn \rightarrow DMGa/DMIn + CH_3$$
 (2)

$$DMGa/DMIn \rightarrow MGa/MIn + CH_3$$
 (3)

$$MGa/MIn \rightarrow Ga/In + CH_3$$
 (4)

Figure 1 indicates that the ReaxFF and DFT energy curves for bond dissociations and angle distortions show good agreement, and ReaxFF successfully reproduces the DFT-based dissociation energies of the reactions in eqs 2–4 (Figure 2a,b).

The carbon parameters originated from the ReaxFF C-2013 force field developed by Srinivasan et al. ⁵⁶ and the extended version by Damirchi et al. ⁵⁷ As such, the adsorption energies of a Ga/In atom on a pristine graphene and a graphene with a monovacancy (MV-Gr) or a divacancy (DV-Gr) were included in two ReaxFF training sets without further modification for carbon parameters. The adsorption energy, $E_{\rm ads}$, of a Ga/In atom on the graphene is computed using

$$E_{\rm ads} = E_{\rm Ga/In + Gr} - (E_{\rm Ga/In} + E_{\rm Gr})$$
 (5)

where $E_{\rm Ga/In+Gr}$ is the total energy of a graphene with a Ga/In atom adsorbed. $E_{\rm Ga/In}$ and $E_{\rm Gr}$ are the energies of an isolated Ga/In atom and a graphene sheet in a vacuum, respectively. As expected, the bond strength of the Ga/In atom on a pristine graphene is significantly weaker than that on MV-Gr and DV-Gr, due to the presence of dangling bonds in defective graphene. As seen from Figure 2c,d, the ReaxFF adsorption energies are in good agreement with the DFT values. Detailed information on the parameterization and validation of the ReaxFF force field (Figure S13) in addition to the GaCH-2020 and InCH-2020 force fields is available in the Supporting Information.

2.3. ReaxFF Molecular Dynamics Simulations. We performed a series of ReaxFF MD-simulations with our newly developed GaCH-2020 and InCH-2020 ReaxFF reactive force fields to study (a) the Ga/In cluster formation from thermal decomposition of TMGa/TMIn gas precursors, (b) the nucleation and growth of Ga/In from an elemental metallic source on monolayer MV-Gr and DV-Gr, and (c) the nucleation and growth of Ga/In from an elemental metallic source on bilayer zigzag-edged graphene (ZZ-Gr) and armchair-edged graphene (AC-Gr).

For case (a), to keep TMGa/TMIn molecules in the gas phase at varying temperatures, we set their densities at 0.019 g/cm³, which are far smaller than those in liquid phases (1.151 and 1.568 g/cm³ at 20 °C for TMGa and TMIn, respectively). To this end, we randomly placed 50 TMGa/TMIn molecules in an 80.00 Å \times 80.00 Å \times 80.00 Å orthogonal simulation box. Following the structural optimization, we equilibrated the system at 300 K with an NVT ensemble for 400 ps. The periodic boundary condition (PBC) was applied to all three directions of the orthogonal simulation box. Then, the entire system was heated up from 300 to 2800 K with a heating rate of 10 K/ps and a timestep of 0.25 fs. The timestep was chosen so that we can simulate the thermal decomposition of TMGa/ TMIn at high temperatures (Figure S14) and the surface reactions with graphene efficiently and with good energy conservation. This procedure adopted a stair-wise heating and annealing, in which 10 ps heating was followed by 10 ps annealing for every 100 K temperature increase. To investigate the temperature effect on the pyrolysis of TMGa/TMIn and the associated Ga/In cluster formation, we further annealed the system at 300, 800, 1300, 1800, 2300, and 2800 K individually for 2000 ps, letting the thermal decomposition fully develop, such that Ga/In atoms from the gas precursors can nucleate and grow to form clusters. To reduce the contamination of the heteroatoms (carbon and hydrogen) in the Ga/In clusters, three methods were employed: the first

method (M_1) is to remove CH_4 gas molecules every 10 ps; the second method (M_2) is to remove CH_4 and CH_3 gas molecules every 10 ps; and the third method (M_3) is to remove gas molecules with the molecular weight $M_w \leq 16$ g/mol every 10 ps. The bond order of the molecule identification was set to be 0.3, which means, for example, that if the bond order of a Ga—H radical is below 0.3, then Ga and H are considered as two individual molecules, and then, the H atom will be removed from the system by utilizing M_3 . These bond order settings are only for post-run molecular analysis and do not affect the actual ReaxFF simulation.

In case (b), two representative models of MV-Gr and DV-Gr were prepared from a pristine graphene containing 180 C atoms by deleting one and two C atoms for MV-Gr and DV-Gr from the center of graphene, respectively. Subsequently, MV-Gr and DV-Gr were placed in the center of a 21.30 Å \times 22.14 Å \times 40.00 Å orthogonal simulation box, so as to meet the PBC in all three directions, as shown in Figure S15a,b. A total of 100 elemental Ga/In atoms were randomly placed in the box or shot from an atom gun⁵⁸ with a velocity of 0.5, 5.0, or 50.0 mm/s along the out-of-plane direction to the center of the graphene to mimic the flux of Ga/In volatile precursors. The vacancies could be either bare (Figure S15a,b) or pre-doped with a single Ga/In atom (Figure S15c,d) to simulate the nucleation and growth of vaporized Ga/In atoms on MV-Gr and DV-Gr.

Case (c) includes a bilayer ZZ-Gr or AC-Gr placed in the center of a 38.34 Å × 39.36 Å × 40.00 Å orthogonal simulation box, in order to meet the PBC in all three directions, as shown in Figure S16a,b. 32 Ga/In atoms were pre-doped evenly on the two zigzag edges of a bilayer graphene consisting of 896 C atoms (Figure S16a), and 18 Ga/In atoms were pre-doped evenly on the two armchair edges of the bilayer graphene consisting of 882 C atoms (Figure S16b). The C atoms at the far end of the bilayer graphene, which are close to the periodic boundaries, were fixed, so that the center of the bottom layer would not move. An additional 100 Ga/In atoms were shot from an atom gun with a shooting velocity of $v_1 = 0.5$ mm/s, $v_2 = 5.0$ mm/s, or $v_3 = 50.0$ mm/s along the out-of-plane direction to the center of the bottom layer of ZZ-Gr and AC-Gr

For cases (b) and (c), we applied similar procedures to case (a), which are structural optimization, equilibration, heating, and annealing, all with a time step of 0.25 fs simulated in an *NVT* ensemble. Nonetheless, the annealing process was slightly different than case (a), for which we only chose 300 and 1000 K as the comparative groups for the temperature effect study. In particular, 100 elemental Ga/In atoms were introduced every 20 ps at 300 and 1000 K during the annealing process. After these elemental metallic atoms were on or around the vacancies or edges, the system was equilibrated further at 300 or 1000 K for 2000 ps, so that the clusters could fully grow. Three different samples (represented by different coordinates and velocities) of each growth condition for cases (a), (b), and (c) were utilized for the statistical calculations.

3. RESULTS AND DISCUSSION

3.1. Ga/In Cluster Formation from TMGa/TMIn Gas Precursors. The inherent presence of C and H atoms is well known in the synthesis of group-III nitrides, resulting from the use of metal—organic precursors. However, the carbon content can be reduced by tuning the growth conditions, such as temperature, pressure, and mixing ratio of gas

precursors for impurity incorporation control. 60,61 In this section, our objective is to achieve optimized conditions for the formation of the Ga/In cluster and further validate the performance of our newly developed force fields by the thermal decomposition of TMGa/TMIn gas precursors without addressing the complex surface/interface chemistry occurring on the substrate. To this end, we apply a temperature annealing treatment at temperatures from 300 to 2800 K. In addition, we employ three hydrocarbon gas removal methods, M₁, M₂, and M₃, as described in Section 2.3, to minimize C and H impurities and expedite the TMGa/TMIn pyrolysis process on a nanosecond time scale. The gas removal methods are analogous to the simplified pathway proposed by Danielsson et al. for obtaining Ga from MGa, by eliminating CH₃ from MGa derivatives that are adsorbed on the surface. 61

As the temperature rises, TMGa/TMIn is thermally decomposed into DMGa/DMIn, then to MGa/MIn, and finally to Ga/In atoms, which provides the basis of Ga/In cluster formation. The schematic of TMGa converting from gas precursors to a Ga cluster under the thermal and gas removal treatments is presented in Figure 3a. As expected, the

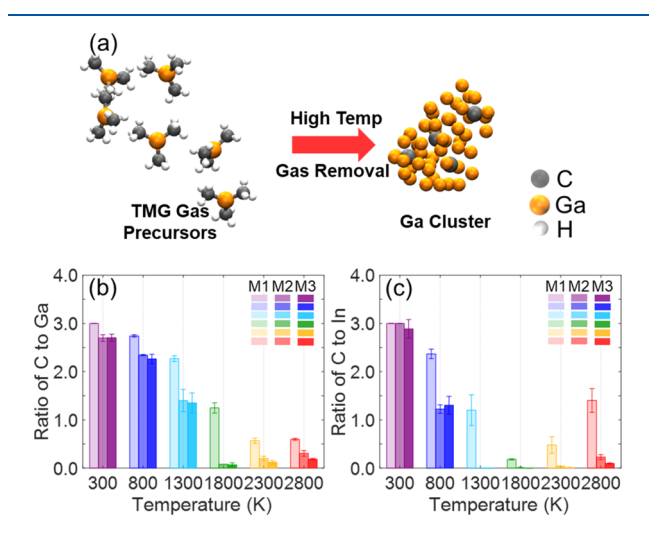


Figure 3. Ga/In cluster formation from TMGa/TMIn gas precursors using the three gas removal methods, M_1 , M_2 , and M_3 , where M_1 is to remove CH₄ gas molecules ever 10 ps, M_2 is to remove CH₄ and CH₃ gas molecules every 10 ps, and M_3 is to remove all gas molecules with the molecular weight $M_w \leq 16$ g/mol every 10 ps. (a) Schematic of Ga clusters dissociated from TMGa gas-phase precursors. Ratios of (b) C to Ga and (c) C to In at the end of the clustering processes at 300, 800, 1300, 1800, 2300, and 2800 K.

heteroatoms, C and H atoms, still reside in the cluster even with a prolonged reaction time, bringing impurity incorporation to the final cluster. Herein, we seek for the optimized conditions, with respect to the selection of the temperature and method for gas removal, aiming to generate Ga/In clusters of a large cluster size yet the least impurities.

Figure 3b,c depicts the ratios of C to Ga and C to In at the end of the clustering processes, such that the lower ratio signifies less C contamination. In comparison with the method M_1 , the methods M_2 and M_3 lead to lower ratios of C to Ga and C to In, which can effectively eliminate the C atoms from clusters. Particularly, at 1800 K, the C to Ga ratios using methods M_2 and M_3 decay to less than 0.1, while the C to In ratios using the methods M_2 and M_3 are below 0.01 and zero. In addition, the ratios of H to Ga and H to C at the end of the

clustering processes are plotted in Figure 4a,b, where very similar trends of H elimination can be observed to those of the

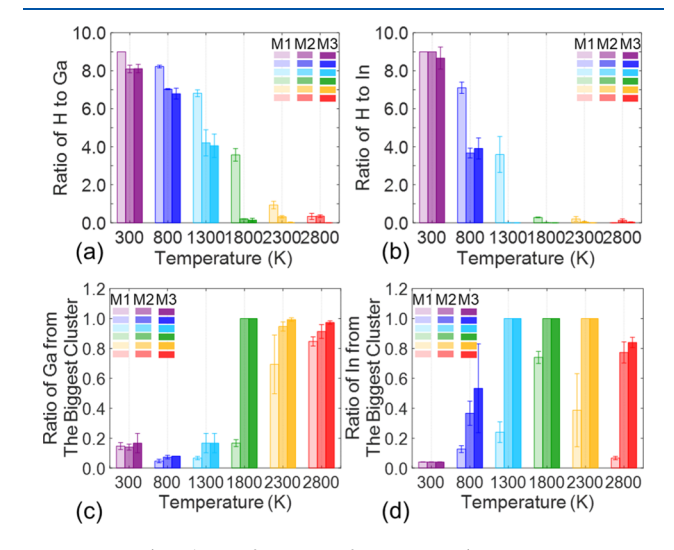


Figure 4. Ga/In cluster formation from TMGa/TMIn gas precursors using the three gas removal methods, M_1 , M_2 , and M_3 , where M_1 is to remove CH₄ gas molecules ever 10 ps, M_2 is to remove CH₄ and CH₃ gas molecules every 10 ps, and M_3 is to remove all gas molecules with the molecular weight $M_{\rm w} \leq 16$ g/mol every 10 ps. Ratios of (a) H to Ga and (b) H to In at the end of clustering processes at 300, 800, 1300, 1800, 2300, and 2800 K; ratios of (c) Ga and (d) In atoms forming the biggest cluster at the end of clustering processes at 300, 800, 1300, 1800, 2300, and 2800 K.

C elimination presented in Figure 3b,c. Furthermore, In clusters tend to contain less or negligible C and H compared with Ga clusters when adopting the methods M₂ and M₃ at temperatures between 1800 and 2800 K, due to the weaker bond strength of methyl groups to In atoms than those to Ga atoms, as also shown in Figure 2a,b. Namely, MGa is more stable than MIn, so MGa radicals are more likely to maintain their structures for a long time and contain more heteroatoms at high temperature. In addition, the MD trajectories also indicate higher production of hydrocarbon radicals and molecules of low molecular weight from TMIn than TMGa during the heating step. For example, $37.33 \pm 1.15\%$ CH₃ radicals dissociate from TMGa at the end of the heating step at 2300 K, whereas $76.00 \pm 1.15\%$ CH₃ radical formation is observed for TMIn at the end of the heating step at 2300 K. As the annealing step begins, both M2 and M3 frequently remove all CH₃ radicals from the TMGa/TMIn systems, so that the carbon content of the TMIn systems can be rapidly reduced, forming In clusters with less C and H concentration compared with those forming from the TMGa systems. However, the low ratios of heteroatoms to Ga/In do not necessarily indicate good quality of the clusters, because the growing Ga/In clusters could melt into smaller clusters containing fewer numbers of Ga/In atoms, losing the covalent character at high temperature.⁶² Accordingly, we normalize the ratios of Ga/In atoms of the biggest cluster in the systems to identify the integrity of the clusters—the ratios are computed by dividing the total number of Ga/In atoms of the biggest cluster by the total number of Ga/In atoms in the system, as shown in Figure 4c,d. The low ratios of Ga atoms in the biggest cluster from 300 to 1300 K indicate the non-completion of the thermal decomposition of gas precursors, regardless of the methods. Nevertheless, the In cluster size reaches the maximum at a lower temperature than the Ga cluster size. However, unlike the growing ratios of the biggest Ga cluster at high temperatures, the ratios of the biggest In cluster decrease to 0.4 at 2300 K and decrease to less than 0.1 at 2800 K, with $\rm M_1$ applied, as depicted in Figure 4c,d. This is because at high temperatures, for example, 2300 and 2800 K, the TMIn molecules quickly disintegrate and lead to the formation of Inand C-containing small compounds and $\rm H_2$ gas molecules, scattering throughout the systems, while the high temperature makes these scattered In- and C-containing compounds more prone to continue melting than clustering. Again, these observations are in accordance with the dissociation energy calculations presented in Figure 2a,b.

We have screened the optimal growth conditions with the selection of the temperature and the gas removal method for Ga/In cluster formation from the pyrolysis of TMGa/TMIn gas precursors, which setting the temperature at 1800 K with the use of the methods M_2 and M_3 , gives the least concentrations of C and H for TMGa/TMIn to generate high-purity Ga/In clusters; meanwhile, the integrity of the Ga/In clusters (corresponding to all Ga/In atoms forming the biggest clusters) is sustained. In addition, the decreasing trend of the carbon concentration of the TMGa systems at high temperatures with the use of the methods M_2 and M_3 is in good agreement with the experimental findings, which indicate that the carbon concentration decays dramatically as the temperature rises above 900 °C (1173 K). 61,63

3.2. Nucleation and Growth of Ga/In from an Elemental Metallic Source on Defective Graphene. Mono- or few-layer graphene can be used as a substrate for the van der Waals epitaxial growth of group-III nitrides.⁶⁴ In Section 3.1, we have identified the thermal decomposition of TMGa/TMIn gas precursors at elevated temperatures and the optimal processing conditions for the Ga/In cluster formation in the absence of substrate. In this section, we skip the thermal decomposition processes of TMGa/TMIn gas precursors; instead, we feed the elemental Ga/In atoms to monolayer MV-Gr and DV-Gr, to examine the growth of Ga/In clusters in the presence of the substrate on the nanosecond time scale. Other accelerating approaches for the cluster growth, such as the introduction of Ga/In-functionalized vacancies and the atom gun toolkit of ADF⁶⁵ that mimics the flux of Ga/In precursors, are also adopted. Graphene may experience topological defects as the temperature goes above 800 °C (1073 K), 66,67 yet considering the fact that the Ga/In cluster could produce premium purity and integrity at a temperature above 1800 K based on Section 3.1, herein, we propose the dual temperature zones for the study of Ga/In cluster formation. As such, a lowtemperature zone is set as 300 K $\leq T \leq$ 1000 K for the Ga/In cluster formation in the presence of the graphene substrate and a high-temperature zone is selected as 1300 K $\leq T \leq$ 1800 K for that in the absence of the graphene substrate. In this section, we choose the lower and upper limits of the low temperature zone, that is, 300 and 1000 K, to examine the temperature effect of the Ga/In nucleation on MV-Gr and DV-Gr.

We calculate the Ga–Ga and In–In RDFs, g(r), as a function of distance, r, for the Ga and In clusters formed at 300 K. The yellow and orange dotted lines represent the first-neighbor distances between Ga atoms, $r_{\rm Ga-Ga}$, and In atoms, $r_{\rm In-In}$, which are 2.71 and 2.97 Å, respectively, as shown in Figure 5j. The values of $r_{\rm Ga-Ga}$ and $r_{\rm In-In}$ are in good agreement with the DFT data published in earlier work. ^{62,68,69} To the best

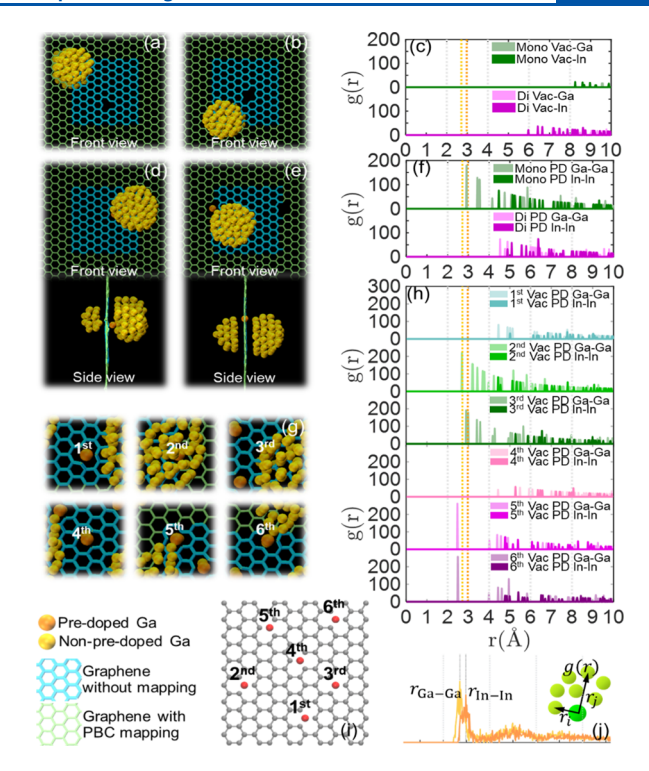


Figure 5. VMD snapshots of Ga and the RDF plots of Ga/In nucleation and growth on a monolayer MV-Gr and DV-Gr. Scheme (i): without pre-doping or an atom gun at T=300 K: Ga nucleation and growth on (a) MV-Gr and (b) DV-Gr; (c) RDF plots of Ga/In nucleation and growth on MV-Gr and a DV-Gr. Scheme (ii): with pre-doping and an atom gun at $v_2=5$ mm/s and T=300 K: Ga nucleating and growth on (d) MV-Gr and (e) DV-Gr; (f) RDF plots of Ga/In nucleation and growth on MV-Gr and DV-Gr. Scheme (iii): with pre-doping and an atom gun on a monolayer graphene with randomly distributed 6 MVs at $v_2=5$ mm/s and T=300 K: (g) Ga nucleation and growth on the 1st to 6th MVs; (h) RDF plots of Ga/In nucleation and growth around the 1st to 6th MVs. (i) Schematic of the locations of the 1st to 6th MVs. (j) RDF plots of Ga and In clusters formed at 300 K, in order to determine the reference peak locations for $r_{\rm Ga-Ga}$ and $r_{\rm In-In}$.

of our knowledge, there is no experimental or theoretical bond lengths for the pure $\rm In_2$ dimer, while the mean values of $r_{\rm In-In}$ from metalloid clusters with an In–In bonded core lay within the range of 2.78–3.15 Å. $^{70-73}$ The first-neighbor distances of a Ga/In cluster can be altered as the structural arrangement transformation and the phase change occur at elevated temperatures. For instance, the structural arrangement of Ga/In clusters could exhibit α -, β -, γ -, and δ -Ga cluster modifications. 69,74 In terms of the temperature effect, Steenbergen and Gaston reported that at low temperature, Ga_n clusters (n=7-12) present unique structural signatures, whereas at high temperature, Ga_n clusters (particularly for n=9-12) demonstrate liquid structures, with $r_{\rm Ga-Ga}$ shifting rightwards on the RDFs from 2.75 to 2.83 Å. 62

Three schemes are incorporated to investigate the nucleation and growth of Ga/In on an MV-Gr and a DV-Gr: (i) elemental Ga/In atoms are randomly placed surrounding MV-Gr and DV-Gr at 300 K, letting the nucleation occur spontaneously, (ii) Ga/In atoms are shot with an atom gun with a shooting velocity of 5 mm/s onto Ga/In-functionalized MV-Gr and DV-Gr at 300 K, and (iii) Ga/In atoms are shot with an atom gun with a shooting velocity of 5 mm/s onto a monolayer graphene with six randomly distributed MVs, each

pre-doped with a Ga/In atoms at 300 K, as shown in Figure 5i. Figure 5a,b,d,e,g displays the MD snapshots, processed using the visualization software VMD, ⁷⁵ of Ga/In clusters that are fully developed under the three schemes. Additionally, the RDFs illustrated in the same figure are computed between the centers of the vacancies and the surrounded Ga/In atoms ($r_{\text{vac-Ga}}$ and $r_{\text{vac-In}}$) for scheme (i) and between the pre-doped and deposited Ga/In atoms from the atom gun ($r_{\text{PD Ga-Ga}}$ and $r_{\text{PD In-In}}$) for scheme (ii) and (iii), in order to quantitatively analyze the growth ratio of Ga/In nuclei, as shown in Figure 5c,f,h.

In scheme (i), the Ga/In atoms are prone to clustering locally and afterwards depositing on the pristine graphene surface, while they have little chance to bind with the MV-Gr and DV-Gr through covalent bonds (Figures 5a,b and S17e,g); thus, no evident peaks occur around the reference lines on the RDF plots (Figure 5c). Although a Ga/In atom absorbed on a pristine graphene has a weaker bond strength (less negative binding energy) than that on an MV or a DV (Figure 2c,d), the much higher probability of the Ga/In atom colliding with the neighboring Ga/In atoms enables the Ga/In cluster formation before arriving in the vicinity of the bare MV or DV. The comparison of the Ga cluster formation on an infinite size graphene (with PBC applied) and a finite size graphene with edges (without PBC applied) can be seen from Figure S18. In this figure, the Ga atoms nucleate on the exposed edges and grow to clusters around the nuclei (Figure S18c,d), regardless of temperature. Nonetheless, when introducing an infinite-size MV-Gr or DV-Gr as a substrate, as a consequence of low probability of being trapped by defects, the Ga clusters are more likely to deposit on the surface via weaker van der Waals interactions, similar to those presented in Figure S18a,b.

In scheme (ii), the majority of Ga atoms nucleate on the pre-doped MV-Gr, as shown in Figure 5d. This can be attributed to the strongest bond strength (the most negative binding energy) of -85.65 kcal/mol for Ga atom with predoped MV-Gr over all the considered scenarios, as indicated in Table S1. In other words, the much stronger interaction of a Ga atom with a pre-doped MV-Gr requires much higher dissociation energy to break the covalent bonds between the deposited and the pre-doped Ga atoms, proving a more stable and directional base for the growth of Ga nuclei. 76 The occurrence of the Ga-Ga first-neighbor peak between the yellow and orange reference lines shown in Figure 5f also supports the fact that the Ga atoms shot with an atom gun prefer to grow around MV, by forming the covalent bonds with the pre-doped Ga atom, despite the slightly different structural arrangement from that formed by the elemental metal source. In contrast, the weaker bond strength (less negative binding energy) of -29.70 kcal/mol for Ga atom with the pre-doped DV-Gr makes the Ga atoms less likely to nucleate around the DV, as shown in Figure 5e. For similar reasons, at a low shooting velocity ($v_1 = 0.5 \text{ mm/s}$), In atoms first form small clusters in a vacuum before reaching the graphene surface, and then, the small clusters deposit on the MV-Gr and DV-Gr and coalesce into a big cluster. At a high shooting velocity ($v_3 = 50$ mm/s), In clusters grow much bigger surrounding the nuclei formed on the surface, moving around MV-Gr and DV-Gr without being trapped by the vacancies. Therefore, no In-In first-neighbor peaks can be seen from the RDF plots, regardless of the type of defects, temperatures, and shooting velocities, as shown in Figures 5f and S19c-h.

From scheme (ii), we reach a conclusion that Gafunctionalized MV-Gr promotes the cluster growth. To take this point further, in scheme (iii), we focus on the defectdriven Ga nucleation and growth in monolayer graphene with six randomly distributed MVs. The existence of multiple MVs could change the structural arrangement of Ga clusters as they nucleate and grow, whereas no In clusters can be found around the pre-doped In atoms through covalent bonds, regardless of temperatures and shooting velocities, due to a much weaker bond strength (less negative binding energy) of -30.21 kcal/mol for an In atom bonding with the pre-doped MV-Gr than the Ga atom case (Table S1). This value shows even weaker bond strength than that of the pristine graphene case, which is about -50 kcal/mol (Figure 2d). In Figure 5g, the Ga cluster is covalently bonded with the second, third, fifth, and sixth MVs. Accordingly, in Figure 5h the first-neighbor peaks of the 5th and 6th MVs occur at a shorter Ga-Ga distance of 2.47 Å than that of the yellow reference line indicates, implicating a possible transformation to a distinct cluster modification realized by only tunning the defects on a graphene. It should be noted that in our MD simulations, the nucleation of Ga atoms takes place at random locations of pre-doped MVs, so that the shapes of Ga clusters could be different from configuration to configuration. However, it is observed that at 300 K, the Ga cluster typically grows around three to four different MVs and yields a more outspread or even a film-like cluster rather than that previously of a spherical shape. This provides the possibility of growing a 2D Ga cluster film with the help of the graphene substrate with multiple Gafunctionalized MVs. Nevertheless, as the temperature rises to 1000 K, only a few Ga-Ga first-neighbor peaks are observed, due to the dislocation of the pre-doped Ga atoms at high temperature, as shown in Figures S20d-f and S17r. Again, no In-In first-neighbor peaks can be seen from the RDF plots, disregarding the type of defects, temperatures, and shooting velocities, as shown in Figure S20.

Based on the analyses above, we have demonstrated that MV-Gr can catalyze the covalent bonding between the predoped and deposited Ga atoms at 300 K, thus increasing the chance of forming nuclei for the directional growth of Ga clusters on MV-Gr. The covalent bonds between the deposited and pre-doped In atoms are barely seen, disregarding the type of defects, temperatures, and shooting velocities of the atom gun. At the temperature of 1000 K, the pre-doped Ga atoms may experience dislocation in the vacancies; therefore, the firstneighbor peaks shift rightwards rather than overlapping the two reference lines. Although the pre-doped In atoms may also undergo dislocation in the vacancies at high temperature, the weak binding energies of -30.21 and -30.51 kcal/mol for an In atom bonding with pre-doped MV-Gr and DV-Gr lead to the In cluster formation away from pre-doped defects, as both binding energies are weaker than those of the pristine case, that is, ~50 kcal/mol, as well. The findings suggest that a Gafunctionalized defective graphene enables us to conduct the directional Ga growth even at room temperature; furthermore, the shape of a grown cluster could be intentionally modified by introducing multiple MVs on a graphene substrate.

3.3. Nucleation and Growth of Ga/In from an Elemental Metallic Source on the Edges of Bilayer Graphene. In this section, we consider bilayer graphene as a substrate along with acceleration approaches for the investigation of the Ga/In nucleation and growth. As shown in Figure S16, the top-layer graphene with ZZ-Gr or AC-Gr is

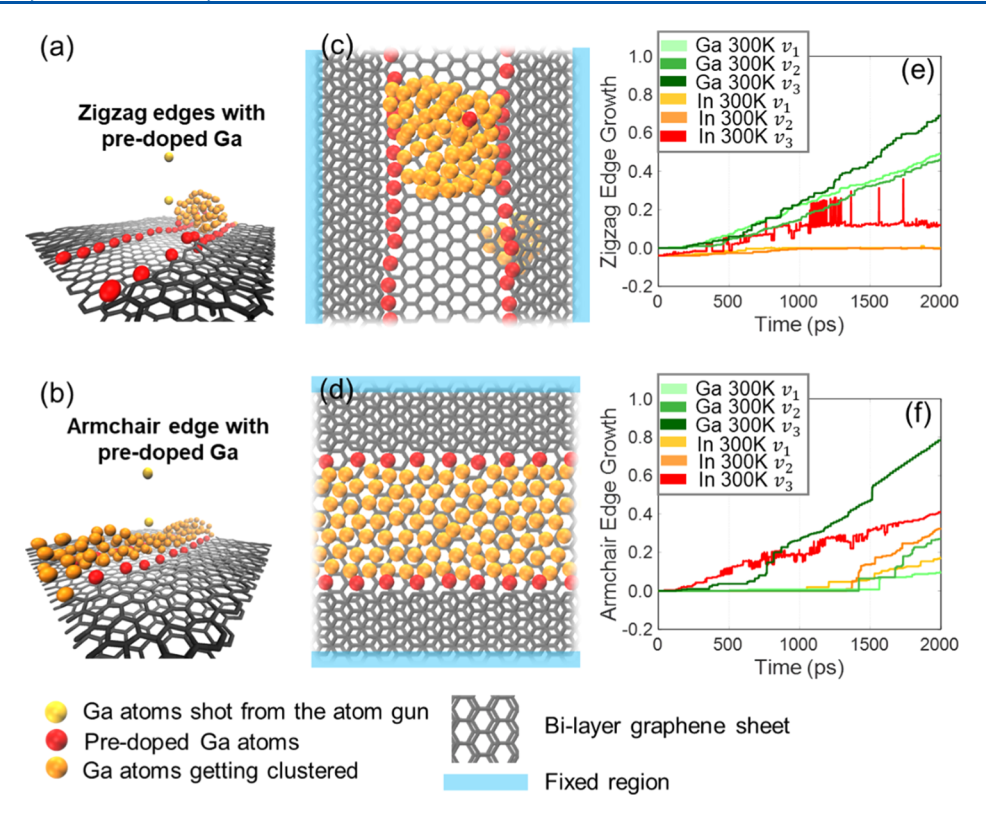


Figure 6. Nucleation and growth of Ga/In from an elemental metal source on a ZZ-Gr and an AC-Gr with pre-doped Ga/In atoms. VMD 3D schematics of the Ga cluster growth on (a) ZZ-Gr and (b) AC-Gr with pre-doped Ga atoms and an atom gun. VMD 2D snapshots of the Ga cluster growth on (c) ZZ-Gr and (d) AC-Gr with pre-doped Ga atoms at T = 1000 K and $v_3 = 50$ mm/s. The ratios of the Ga/In cluster growing on (e) ZZ-Gr and (f) AC-Gr at T = 300 K and at shooting velocities of $v_1 = 0.5$ mm/s, $v_2 = 5$ mm/s, and $v_3 = 50$ mm/s. The curves from (e,f) are plotted by the mean values of 3 samples, but the standard deviations are not shown for clarity.

functionalized with Ga/In atoms to initiate and catalyze the kink nucleation for the cluster growth; meanwhile, the bottom layer confines and shapes the thin-layer growth of Ga/In clusters and, in practical application, serves as a buffer layer to ensure the van der Waals growth. 69 Similar to the cases presented in Section 3.2, we employ the lower and upper limits of the low-temperature zone, 300 and 1000 K, to inspect the temperature effect on the Ga/In thin-film growth, initiating from ZZ-Gr and AC-Gr, and to prevent the deterioration of graphene at high temperature. ^{59,60} We identify that the nucleation of Ga/In atoms on the bare edges only leads to a spherical or quasi-spherical shape cluster for ZZ-Gr and AC-Gr, as shown in Figure S21. Therefore, we propose a predoped ZZ-Gr and AC-Gr as a substrate, in which the uncoordinated C atoms on the edges are fully passivated by Ga/In atoms that could act as pre-existing nuclei for the subsequent thin-layer growth. Then, the Ga/In atoms are shot from an atom gun at three constant velocities, that is, $v_1 = 0.5$ mm/s, $v_2 = 5$ mm/s, and $v_3 = 50$ mm/s, onto the center of the pre-doped ZZ-Gr and AC-Gr, as shown in Figure 6a,b, respectively.

At a low shooting velocity, the Ga/In atoms nucleate in a vacuum or around the pre-doped Ga/In atoms and then grow into bigger clusters; at a high shooting velocity, the initial Ga/In atoms shot onto the bottom layer bounce around between the edges of ZZ-Gr and AC-Gr, and then, they start to bind with the pre-doped Ga/In atoms and serve as nuclei for the subsequent cluster growth.

To quantify the impact of temperature and shooting velocity on the Ga/In clusters grown on ZZ-Gr and AC-Gr, we further compute the growth ratios of Ga/In clusters, each including 100 atoms shot with an atom gun, over the clustering elapsed time of 2000 ps, as shown in Figures 6e,f and S22a,b. Note that the growth ratio is defined as the total number of Ga/In atoms in a cluster that is covalently bound to the pre-doped edges divided by the total number of Ga/In atoms in a whole system. The increase in the shooting velocity promotes the nucleation and growth of Ga/In metals on edges, except for the Ga/In clusters growing on the ZZ-Gr at ν_1 and ν_2 , which present nearly the same mean growth ratios during the clustering process. In comparison with Ga, In exhibits a much lower rate of nucleation and growth ratio, regardless of temperatures and shooting velocities.

We acquire two observations from the MD trajectories: (1) the pre-doped In atoms on ZZ-Gr tend to follow a staggered arrangement (Figure S23m-r), which may result in the oncoming In atoms hardly growing on the ZZ-Gr; (2) the In atoms only regionally nucleate and grow on AC-Gr, forming a smaller 3D cluster than that growing on the Ga-functionalized AC-Gr. For observation (1), recall that in Section 3.2, the $r_{\text{In-In}}$ value is derived to be 2.97 Å, which is 0.53 Å larger than the spacing between the two doping sites on the ZZ-Gr, hence the notable rearrangement of pre-doped In atoms in a staggered pattern on the ZZ-Gr. In addition, based on our ReaxFF energy calculations, the potential energy of a minimized ZZ-Gr with pre-doped In atoms in a staggered pattern is about 1500 kcal/mol lower (more negative) than that in an organized pattern, not energetically favored to the formation of In clusters through covalent bonds as well. On the other hand, as we inspect the clustering time for 100 separate Ga/In atoms evolving into a big cluster, In atoms take significantly shorter time than Ga atoms in the temperature range of 300-1000 K, as shown in Figure S24. In other words, the In atoms, compared with the Ga atoms, should have a better chance to nucleate before reaching the AC-Gr surface, especially at a low temperature and a low shooting velocity. These could be the reasons responsible for a much lower rate of nucleation and growth ratio of In atoms from our observation. Higher temperature increases the mobility of Ga/In gas-phase precursors and contributes to a fast and more extensive cluster growth, where coagulation and coalescence could occur rapidly. For example, comparing Figure 6f with Figure S22b, the growth ratio of the Ga cluster on AC-Gr at the end of the clustering process is enhanced by 0.18-0.61 at varying velocities, as the temperature goes from 300 to 1000 K. It is noteworthy that the growth ratio of the Ga cluster at v_3 on AC-Gr increases from 0.80 at 300 K to 1.00 at 1000 K, at the end of the second equilibration process after the clustering stage, as shown in Figure S22d. There are other parameters that could affect the growth ratio of Ga/In clusters, such as pressure, the density of gas precursors, the geometries of substrate, and so forth. We point out the effect of the width between the two edges of ZZ-Gr and AC-Gr, as shown in Figure S25, to our readers, but in this paper, we will not discuss any of these parameters in more detail.

Generally, a higher temperature and a higher shooting velocity can bring about a higher growth ratio for the Ga/In cluster. However, a higher growth ratio only reflects a higher degree of Ga/In cluster formation on the ZZ-Gr and AC-Gr, yet the growth pattern cannot be adequately indicated. For instance, the Ga clusters on ZZ-Gr exhibit higher growth ratios at v_1 and v_2 than those on AC-Gr (Figure 6e,f), whereas the Ga cluster growth on ZZ-Gr is neither a 3D spherical cluster nor a 2D thin-layer cluster; instead, the Ga atoms are merely individually bound by the pre-doped Ga atoms on the ZZ-Gr. Another case in point is that the In clusters display higher growth ratios with notable spikes at v_3 than those at v_1 or v_2 (Figures 6e,f and S22a,b). However, this does not represent good quality for the In cluster growth either, due to the unstable kinetics at this high shooting velocity. Therefore, we profile the geometries of the fully grown Ga/In clusters on ZZ-Gr and AC-Gr at different temperatures and shooting velocities (Figure S23), and then, we select the cases of our interest, Ga cluster growth at v_3 , to plot the Ga-edge distributions against the left and right edges for ZZ-Gr and against the top and bottom edges for AC-Gr, as shown in Figure S26.

In Figure 6c,d, we present the two types of cluster formation, for 100 Ga atoms growing on a ZZ-Gr and an AC-Gr with T =1000 K and $v_3 = 50$ mm/s. At this particular temperature and shooting velocity, Ga atoms manifest a 3D cluster growth on ZZ-Gr (Figure 6c), while the AC-Gr is more prone to promoting a 2D thin-layer cluster growth (Figure 6d). This could result from the smaller spacing between each two predoped Ga atoms on the ZZ-Gr than that between each two pre-doped Ga atoms on the AC-Gr, which promotes the vertical growth of Ga atoms on the ZZ-Gr. In contrast, the predoped edges of the AC-Gr exert larger spacing between each two pre-doped Ga atoms, making it possible for the oncoming Ga atoms to grow in the lateral direction through covalent bonds. As shown in Figure S23a-l, the ZZ-Gr and AC-Gr both favor the growth of Ga clusters—as shooting velocity increases, the Ga clusters grow bigger; as temperature rises, the Ga clusters are more outspread. Nonetheless, as we have

mentioned previously, In clusters can barely grow on the ZZ-Gr due to the staggered arrangement of the pre-doped In atoms and those on the AC-Gr appear to be more regional and smaller compared with Ga clusters, as can be seen from Figure S23m-x.

In Figure S22c,d, the Ga clusters on the ZZ-Gr and AC-Gr at 1000 K with v_3 both present a growth ratio of 1.0. However, in Figure S26c, the Ga cluster on the ZZ-Gr goes with a 3D growth pattern, yet in Figure S26g, the Ga cluster on the AC-Gr favors a 2D thin-layer growth. As a result, the Ga-edge distribution for the former growth is more outspread, as shown in Figure S26d, whereas the Ga-edge distribution for the latter growth has several characteristic peaks, indicating the periodicity of a 2D thin-layer arrangement, despite the dissociation of one pre-doped Ga atom, as shown in Figure S26h. The Ga cluster has less extended growth at 300 K. In particular, Ga atoms stack on top of one another along the two edges of the ZZ-Gr but coagulate, as shown in Figure S26a, while on the AC-Gr, Ga atoms cannot sufficiently spread out between the edges like those at 1000 K, as shown in Figure S26f.

The above analyses indicate that a combination of T=1000 K and $\nu_2=5$ mm/s or $\nu_3=50$ mm/s could give the best performance for the Ga clusters grown on an AC-Gr, for it not only exhibits the highest growth ratio with the Ga cluster covalently bonded with the pre-doped Ga atoms but also produces a 2D thin-layer between edges without deteriorating the bilayer graphene. However, setting T=300 K for the Ga cluster growth or including the In-functionalized AC-Gr at 1000 K only results in a 3D growth.

4. CONCLUSIONS

We have developed ReaxFF reactive force fields for Ga/C/H and In/C/H systems (GaCH-2020 and InCH-2020), by focusing on the gas-phase reactions of the Ga and In film growth from trimethylgallium (TMGa) and trimethylindium (TMIn) precursors and the surface interactions of TMGa and TMIn with a graphene substrate in metal—organic chemical vapor deposition (MOCVD).

We have identified optimized conditions to obtain Ga/In nanoclusters with low impurities by thermal decomposition of TMGa/TMIn. Based on our molecular dynamics (MD) simulations, the removal of CH₄ and CH₃ every 10 ps (method M₂) or the removal of gas molecules with the molecular weight $M_{\rm w} \le 16$ g/mol every 10 ps (method M₃) at 1800 K leads to Ga/In nanoclusters with the lowest impurities. This result may be transferred to the application of adduct removal from an MOCVD chamber (i.e., CH3 or CH4) to be able to reduce the contamination in Ga/In clusters. Our work demonstrates that Ga-doped monovacancy graphene is more energetically favored for the nucleation of Ga nanoclusters compared with pristine graphene due to a stronger bond strength (more negative binding energy). However, in the In cases, covalent bonds can be barely observed between the In clusters and the pre-doped In atoms, resulting from the weaker bond strength than the Ga equivalents. In addition, our investigation of the growth pattern of Ga nanoclusters and two-dimensional (2D) Ga layers on a bilayer graphene reveals that the armchair edges promote the 2D growth. In future studies, we will seek to extend these ReaxFF reactive force fields towards systems containing nitrides to further investigate the coupled effects of vacancy defects with various sizes and nitrogen species on the growth kinetics of group-III nitrides.

ASSOCIATED CONTENT

Supporting Information

The Supporting Information is available free of charge at https://pubs.acs.org/doi/10.1021/acs.jpcc.1c01965.

Additional comparison between DFT and ReaxFF energies for GaCH-2020 and InCH-2020 ReaxFF force fields developed in this study, flowchart algorithm of ReaxFF force field parameterization and validation, and additional MD Simulations using GaCH-2020 and InCH-2020 ReaxFF force fields (PDF)

AUTHOR INFORMATION

Corresponding Author

Adri C. T. van Duin — Department of Chemical Engineering, Center for Two-Dimensional and Layered Materials (2DLM), Material Research Institute, Department of Mechanical Engineering, Two-Dimensional Crystal Consortium (2DCC), Material Research Institute, and Department of Materials Science and Engineering, The Pennsylvania State University, University Park, Pennsylvania 16802, United States; Orcid.org/0000-0002-3478-4945; Email: acv13@psu.edu

Authors

Siavash Rajabpour — Department of Chemical Engineering and Center for Two-Dimensional and Layered Materials (2DLM), Material Research Institute, The Pennsylvania State University, University Park, Pennsylvania 16802, United States; orcid.org/0000-0002-1686-065X

Qian Mao – Department of Mechanical Engineering, The Pennsylvania State University, University Park, Pennsylvania 16802, United States

Nadire Nayir — Department of Mechanical Engineering and Two-Dimensional Crystal Consortium (2DCC), Material Research Institute, The Pennsylvania State University, University Park, Pennsylvania 16802, United States; Department of Physics, Karamanoglu Mehmetbey University, Karaman 70000, Turkey; orcid.org/0000-0002-3621-2481

Joshua A. Robinson — Center for Two-Dimensional and Layered Materials (2DLM), Material Research Institute, Two-Dimensional Crystal Consortium (2DCC), Material Research Institute, and Department of Materials Science and Engineering, The Pennsylvania State University, University Park, Pennsylvania 16802, United States

Complete contact information is available at: https://pubs.acs.org/10.1021/acs.jpcc.1c01965

Author Contributions

S.R. and Q.M. contributed equally.

Notes

The authors declare no competing financial interest.

ACKNOWLEDGMENTS

The authors acknowledge the funding from the National Science Foundation (NSF), the Division of Materials Research through award number DMR-1808900, the Penn State MRSEC-Center for Nanoscale Science under award number DMR-2011839, the 2D Crystal Consortium NSF Materials Innovation Platform (2DCC-MIP NSF) under cooperative agreement DMR-1539916, and Air Force Office of Scientific Research (AFOSR) grant FA9550-19-1-0295.

REFERENCES

- (1) Nakamura, S.; Senoh, M.; Nagahama, S.-i.; Iwasa, N.; Yamada, T.; Matsushita, T.; Kiyoku, H.; Sugimoto, Y. InGaN-Based Multi-Quantum-Well-Structure Laser Diodes. *Jpn. J. Appl. Phys.* **1996**, 35, L74–L76.
- (2) Nakamura, S.; Mukai, T.; Senoh, M. High-brightness InGaN/AlGaN double-heterostructure blue-green-light-emitting diodes. *J. Appl. Phys.* **1994**, *76*, 8189–8191.
- (3) Nakamura, S.; Krames, M. R. History of Gallium-Nitride-Based Light-Emitting Diodes for Illumination. *Proc. IEEE* **2013**, *101*, 2211–2220.
- (4) Kneissl, M; Kolbe, T; Chua, C; Kueller, V; Lobo, N; Stellmach, J; Knauer, A; Rodriguez, H; Einfeldt, S; Yang, Z; Johnson, N M; Weyers, M; et al. Advances in Group III-Nitride-Based Deep UV Light-Emitting Diode Technology. Semicond. Sci. Technol. 2011, 26, 014036.
- (5) Binari, S. C.; Redwing, J. M.; Kelner, G.; Kruppa, W. AlGaN/GaN HEMTs Grown on SIC Substrates. *Electron. Lett.* **1997**, 33, 242–243.
- (6) Mishra, U. K.; Parikh, P.; Yi-Feng Wu, Y. F. AlGaN/GaN HEMTs-an overview of device operation and applications. *Proc. IEEE* **2002**, *90*, 1022–1031.
- (7) Zhang, J. X.; Qu, Y.; Chen, Y. Z.; Uddin, A.; Yuan, S. Structural and optical characterization of GaN epilayers grown on Si(111) substrates by hydride vapor-phase epitaxy. *J. Cryst. Growth* **2005**, 282, 137–142.
- (8) Hemmingsson, C.; Paskov, P. P.; Pozina, G.; Heuken, M.; Schineller, B.; Monemar, B. Hydride Vapour Phase Epitaxy Growth and Characterization of Thick GaN Using a Vertical HVPE Reactor. *J. Cryst. Growth* **2007**, *300*, 32–36.
- (9) Ponce, F. A.; Krusor, B. S.; Major, J. S.; Plano, W. E.; Welch, D. F. Microstructure of GaN Epitaxy on SiC Using AlN Buffer Layers. *Appl. Phys. Lett.* **1995**, *67*, 410.
- (10) Nakamura, S. The Roles of Structural Imperfections in InGaN-Based Blue Light-Emitting Diodes and Laser Diodes. *Science* **1998**, 281, 956–961
- (11) Schubert, M. F.; Chhajed, S.; Kim, J. K.; Schubert, E. F.; Koleske, D. D.; Crawford, M. H.; Lee, S. R.; Fischer, A. J.; Thaler, G.; Banas, M. A. Effect of Dislocation Density on Efficiency Droop in GaInNGaN Light-Emitting Diodes. *Appl. Phys. Lett.* **2007**, *91*, 231114.
- (12) Rosner, S. J.; Carr, E. C.; Ludowise, M. J.; Girolami, G.; Erikson, H. I. Correlation of Cathodoluminescence Inhomogeneity with Microstructural Defects in Epitaxial GaN Grown by Metalorganic Chemical-Vapor Deposition. *Appl. Phys. Lett.* **1997**, *70*, 420–422.
- (13) Sugahara, T.; Sato, H.; Hao, M.; Naoi, Y.; Kurai, S.; Tottori, S.; Yamashita, K.; Nishino, K.; Romano, L. T.; Sakai, S. Direct Evidence That Dislocations Are Non-Radiative Recombination Centers in GaN. *Jpn. J. Appl. Phys.* **1998**, *37*, L398–L400.
- (14) Ueno, K.; Abe, H.; Saiki, K.; Koma, A. Heteroepitaxy of Layered Semiconductor GaSe on a GaAs(III)B Surface. *Jpn. J. Appl. Phys.* **1991**, *30*, L1352–L1354.
- (15) Liu, K. Y.; Ueno, K.; Fujikawa, Y.; Saiki, K.; Koma, A. Heteroepitaxial Growth of Layered Semiconductor GaSe on a Hydrogen-Terminated Si(111) Surface. *Jpn. J. Appl. Phys.* **1993**, 32, L434–L437.
- (16) Tada, H.; Kawaguchi, T.; Koma, A. Epitaxial Growth of Vanadyl- Phthalocyanine Ultrathin Films on Hydrogen-Terminated Si(111) Surfaces. *Appl. Phys. Lett.* **1992**, *61*, 2021.
- (17) Yamamoto, H.; Tada, H.; Kawaguchi, T. Epitaxial Growth of Metal-Phthalocyanines on Selenium-Terminated GaAs (111) Surfaces. *Appl. Phys. Lett.* **1994**, *64*, 2099.
- (18) Geim, A. K.; Grigorieva, I. V. Van Der Waals Heterostructures. *Nature* **2013**, 499, 419.
- (19) Butler, S. Z.; Hollen, S. M.; Cao, L.; Cui, Y.; Gupta, J. A.; Gutiérrez, H. R.; Heinz, T. F.; Hong, S. S.; Huang, J.; Ismach, A. F.; et al. Progress, Challenges, and Opportunities in Two-Dimensional Materials beyond Graphene. *ACS Nano* **2013**, *7*, 2898.

- (20) Al Balushi, Z. Y.; Miyagi, T.; Lin, Y.-C.; Wang, K.; Calderin, L.; Bhimanapati, G.; Redwing, J. M.; Robinson, J. A. The Impact of Graphene Properties on GaN and AlN Nucleation. *Surf. Sci.* **2015**, 634, 81–88.
- (21) Qi, Y.; Wang, Y.; Pang, Z.; Dou, Z.; Wei, T.; Gao, P.; Zhang, S.; Xu, X.; Chang, Z.; Deng, B.; et al. Fast Growth of Strain-Free AlN on Graphene-Buffered Sapphire. *J. Am. Chem. Soc.* **2018**, *140*, 11935—11941.
- (22) Liang, D.; Wei, T.; Wang, J.; Li, J. Quasi van Der Waals Epitaxy Nitride Materials and Devices on Two Dimension Materials. *Nano Energy* **2020**, *69*, 104463.
- (23) Chen, Z.; Zhang, X.; Dou, Z.; Wei, T.; Liu, Z.; Qi, Y.; Ci, H.; Wang, Y.; Li, Y.; Chang, H.; et al. High-Brightness Blue Light-Emitting Diodes Enabled by a Directly Grown Graphene Buffer Layer. Adv. Mater. 2018, 30, 1801608.
- (24) Munshi, A. M.; Dheeraj, D. L.; Fauske, V. T.; Kim, D.-C.; Van Helvoort, A. T. J.; Fimland, B.-O.; Weman, H. Vertically Aligned GaAs Nanowires on Graphite and Few-Layer Graphene: Generic Model and Epitaxial Growth. *Nano Lett.* **2012**, *12*, 4570–4576.
- (25) Alaskar, Y.; Arafin, S.; Lin, Q.; Wickramaratne, D.; McKay, J.; Norman, A. G.; Zhang, Z.; Yao, L.; Ding, F.; Zou, J.; et al. Theoretical and Experimental Study of Highly Textured GaAs on Silicon Using a Graphene Buffer Layer. *J. Cryst. Growth* **2015**, 425, 268–273.
- (26) Sarau, G.; Heilmann, M.; Latzel, M.; Tessarek, C.; Christiansen, S. GaN-Based Nanorods/Graphene Heterostructures for Optoelectronic Applications. *Phys. Status Solidi B* **2019**, 256, 1800454.
- (27) Wang, Y.; Dheeraj, D.; Liu, Z.; Liang, M.; Li, Y.; Yi, X.; Wang, J.; Li, J.; Weman, H. AlGaN Nanowires Grown on SiO2/Si (100) Using Graphene as a Buffer Layer. *Cryst. Growth Des.* **2019**, *19*, 5516–5522.
- (28) Fernández-Garrido, S.; Ramsteiner, M.; Gao, G.; Galves, L. A.; Sharma, B.; Corfdir, P.; Calabrese, G.; De Souza Schiaber, Z.; Pfüller, C.; Trampert, A.; et al. Molecular Beam Epitaxy of GaN Nanowires on Epitaxial Graphene. *Nano Lett.* **2017**, *17*, 5213–5221.
- (29) Al Balushi, Z. Y.; Wang, K.; Ghosh, R. K.; Vilá, R. A.; Eichfeld, S. M.; Caldwell, J. D.; Qin, X.; Lin, Y.-C.; Desario, P. A.; Stone, G.; et al. Two-Dimensional Gallium Nitride Realized via Graphene Encapsulation. *Nat. Mater.* **2016**, *15*, 1166–1171.
- (30) Sankaranarayanan, S.; Kandasamy, P.; Raju, R.; Krishnan, B. Fabrication of Gallium Nitride and Nitrogen Doped Single Layer Graphene Hybrid Heterostructures for High Performance Photodetectors. Sci. Rep. 2020, 10, 14507.
- (31) Sangiovanni, D. G.; Gueorguiev, G. K.; Kakanakova-Georgieva, A. Ab Initio Molecular Dynamics of Atomic-Scale Surface Reactions: Insights into Metal Organic Chemical Vapor Deposition of AlN on Graphene. *Phys. Chem. Chem. Phys.* **2018**, 20, 17751–17761.
- (32) Zhao, Z.; Bai, P.; Li, L.; Li, J.; Wu, L.; Huo, P.; Tan, L. The Reaction Thermodynamics during Plating Al on Graphene Process. *Materials* **2019**, *12*, 330.
- (33) van Duin, A. C. T.; Dasgupta, S.; Lorant, F. ReaxFF: A Reactive Force Field for Hydrocarbons. *J. Phys. Chem. A* **2001**, *105*, 9396–9409.
- (34) Tersoff, J. Empirical Interatomic Potential for Carbon, with Applications to Amorphous Carbon. *Phys. Rev. Lett.* **1988**, *61*, 2879–2882
- (35) Zheng, Y.; Hong, S.; Psofogiannakis, G.; Rayner, G. B.; Datta, S.; Van Duin, A. C. T.; Engel-Herbert, R. Modeling and in Situ Probing of Surface Reactions in Atomic Layer Deposition. *ACS Appl. Mater. Interfaces* **2017**, *9*, 15848–15856.
- (36) Liu, S.; Van Duin, A. C. T.; Van Duin, D. M.; Liu, B.; Edgar, J. H. Atomistic Insights into Nucleation and Formation of Hexagonal Boron Nitride on Nickel from First-Principles-Based Reactive Molecular Dynamics Simulations. *ACS Nano* **2017**, *11*, 3585–3596.
- (37) Nayir, N.; Van Duin, A. C. T.; Erkoc, S. Development of a ReaxFF Reactive Force Field for Interstitial Oxygen in Germanium and Its Application to GeO2/Ge Interfaces. *J. Phys. Chem. C* **2019**, 123, 1208–1218.

- (38) Nayir, N.; Van Duin, A. C. T.; Erkoc, S. Development of the ReaxFF Reactive Force Field for Inherent Point Defects in the Si/Silica System. *J. Phys. Chem. A* **2019**, *123*, 4303–4313.
- (39) Ostadhossein, A.; Rahnamoun, A.; Wang, Y.; Zhao, P.; Zhang, S.; Crespi, V. H.; Van Duin, A. C. T. ReaxFF Reactive Force-Field Study of Molybdenum Disulfide (MoS2). *J. Phys. Chem. Lett.* **2017**, *8*, 631–640.
- (40) Lotfi, R.; Naguib, M.; Yilmaz, D. E.; Nanda, J.; Van Duin, A. C. T. A comparative study on the oxidation of two-dimensional Ti3C2MXene structures in different environments. *J. Mater. Chem. A* **2018**, *6*, 12733–12743.
- (41) Sang, X.; Xie, Y.; Yilmaz, D. E.; Lotfi, R.; Alhabeb, M.; Ostadhossein, A.; Anasori, B.; Sun, W.; Li, X.; Xiao, K.; et al. In Situ Atomistic Insight into the Growth Mechanisms of Single Layer 2D Transition Metal Carbides. *Nat. Commun.* **2018**, *9*, 2266.
- (42) Nayir, N.; Wang, Y.; Shabnam, S.; Hickey, D. R.; Miao, L.; Zhang, X.; Bachu, S.; Alem, N.; Redwing, J.; Crespi, V. H.; et al. Modeling for Structural Engineering and Synthesis of Two-Dimensional WSe2 Using a Newly Developed ReaxFF Reactive Force Field. *J. Phys. Chem. C* **2020**, *124*, 28285–28297.
- (43) Xuan, Y.; Jain, A.; Zafar, S.; Lotfi, R.; Nayir, N.; Wang, Y.; Choudhury, T. H.; Wright, S.; Feraca, J.; Rosenbaum, L.; et al. Multi-Scale Modeling of Gas-Phase Reactions in Metal-Organic Chemical Vapor Deposition Growth of WSe2. *J. Cryst. Growth* **2019**, 527, 125247.
- (44) Rajabpour, S.; Mao, Q.; Gao, Z.; Khajeh Talkhoncheh, M.; Zhu, J.; Schwab, Y.; Kowalik, M.; Li, X.; van Duin, A. C. T. Low-temperature carbonization of polyacrylonitrile/graphene carbon fibers: A combined ReaxFF molecular dynamics and experimental study. *Carbon* **2021**, *174*, 345–356.
- (45) Kowalik, M.; Ashraf, C.; Damirchi, B.; Akbarian, D.; Rajabpour, S.; van Duin, A. C. T. Atomistic Scale Analysis of the Carbonization Process for C/H/O/N-Based Polymers with the ReaxFF Reactive Force Field. *J. Phys. Chem. B* **2019**, *123*, 5357–5367.
- (46) Zhang, L.; Kowalik, M.; Gao, Z.; Ashraf, C. M.; Rajabpour, S.; Bumgardner, C.; Schwab, Y.; Damirchi, B.; Zhu, J.; Akbarian, D.; et al. Converting PBO Fibers into Carbon Fibers by Ultrafast Carbonization. *Carbon* **2020**, *159*, 432–442.
- (47) Mao, Q.; Rajabpour, S.; Kowalik, M.; van Duin, A. C. T. Predicting cost-effective carbon fiber precursors: Unraveling the functionalities of oxygen and nitrogen-containing groups during carbonization from ReaxFF simulations. *Carbon* **2020**, *159*, 25–36.
- (48) Gao, Z.; Zhu, J.; Rajabpour, S.; Joshi, K.; Kowalik, M.; Croom, B.; Schwab, Y.; Zhang, L.; Bumgardner, C.; Brown, K. R.; et al. Graphene Reinforced Carbon Fibers. *Sci. Adv.* **2020**, *6*, No. eaaz4191.
- (49) Achtyl, J. L.; Unocic, R. R.; Xu, L.; Cai, Y.; Raju, M.; Zhang, W.; Sacci, R. L.; Vlassiouk, I. V.; Fulvio, P. F.; Ganesh, P.; et al. Aqueous Proton Transfer across Single-Layer Graphene. *Nat. Commun.* **2015**, *6*, 6539.
- (50) Bochevarov, A. D.; Harder, E.; Hughes, T. F.; Greenwood, J. R.; Braden, D. A.; Philipp, D. M.; Rinaldo, D.; Halls, M. D.; Zhang, J.; Friesner, R. A. Jaguar: A high-performance quantum chemistry software program with strengths in life and materials sciences. *Int. J. Quantum Chem.* **2013**, *113*, 2110–2142.
- (51) Giannozzi, P.; Baroni, S.; Bonini, N.; Calandra, M.; Car, R.; Cavazzoni, C.; Ceresoli, D.; Chiarotti, G. L.; Cococcioni, M.; Dabo, I.; et al. QUANTUM ESPRESSO: A Modular and Open-Source Software Project for Quantum Simulations of Materials. *J. Phys. Condens. Matter* **2009**, *21*, 395502.
- (52) Blöchl, P. E. Projector Augmented-Wave Method. *Phys. Rev. B: Condens. Matter Mater. Phys.* **1994**, *50*, 17953–17979.
- (53) Kresse, G.; Joubert, D. From Ultrasoft Pseudopotentials to the Projector Augmented-Wave Method. *Phys. Rev. B: Condens. Matter Mater. Phys.* **1999**, *59*, 1758–1775.
- (54) Perdew, J. P.; Burke, K.; Ernzerhof, M. Generalized Gradient Approximation Made Simple. *Phys. Rev. Lett.* **1996**, *77*, 3865–3868.
- (55) Marzari, N.; Vanderbilt, D.; De Vita, A.; Payne, M. C. Thermal Contraction and Disordering of the Al(110) Surface. *Phys. Rev. Lett.* **1999**, 82, 3296–3299.

- (56) Srinivasan, S. G.; Van Duin, A. C. T.; Ganesh, P. Development of a ReaxFF Potential for Carbon Condensed Phases and Its Application to the Thermal Fragmentation of a Large Fullerene. *J. Phys. Chem. A* **2015**, *119*, 571–580.
- (57) Damirchi, B.; Radue, M.; Kanhaiya, K.; Heinz, H.; Odegard, G. M.; Van Duin, A. C. T. ReaxFF Reactive Force Field Study of Polymerization of a Polymer Matrix in a Carbon Nanotube-Composite System. *J. Phys. Chem. C* **2020**, *124*, 20488–20497.
- (58) SCM. SCM ReaxFF Manual ADF Modeling Suite 2018, 2018.
- (59) Koleske, D. D.; Wickenden, A. E.; Henry, R. L.; Twigg, M. E. Influence of MOVPE Growth Conditions on Carbon and Silicon Concentrations in GaN. *J. Cryst. Growth* **2002**, *242*, 55–69.
- (60) Ishibashi, A.; Takeishi, H.; Mannoh, M.; Yabuuchi, Y.; Ban, Y. Residual Impurities in GaN/Al2O3 Grown by Metalorganic Vapor Phase Epitaxy. *J. Electron. Mater.* **1996**, 25, 799–803.
- (61) Danielsson, Ö.; Li, X.; Ojamäe, L.; Janzén, E.; Pedersen, H.; Forsberg, U. A Model for Carbon Incorporation from Trimethyl Gallium in Chemical Vapor Deposition of Gallium Nitride. *J. Mater. Chem. C* **2016**, *4*, 863–871.
- (62) Steenbergen, K. G.; Gaston, N. First-Principles Melting of Gallium Clusters down to Nine Atoms: Structural and Electronic Contributions to Melting. *Phys. Chem. Chem. Phys.* **2013**, *15*, 15325–15332.
- (63) Ciarkowski, T.; Allen, N.; Carlson, E.; McCarthy, R.; Youtsey, C.; Wang, J.; Fay, P.; Xie, J.; Guido, L. Connection between Carbon Incorporation and Growth Rate for GaN Epitaxial Layers Prepared by OMVPE. *Materials* **2019**, *12*, 2455.
- (64) Xu, Y.; Cao, B.; Li, Z.; Zheng, S.; Cai, D.; Wang, M.; Zhang, Y.; Wang, J.; Wang, C.; Xu, K. A Self-Assembled Graphene Nanomask for the Epitaxial Growth of Nonplanar and Planar GaN. *CrystEngComm* **2019**, *21*, 6109–6117.
- (65) te Velde, G.; Bickelhaupt, F. M.; Baerends, E. J.; Fonseca Guerra, C.; van Gisbergen, S. J. A.; Snijders, J. G.; Ziegler, T. Chemistry with ADF. *J. Comput. Chem.* **2001**, *22*, 931–967.
- (66) Gong, C.; He, K.; Chen, Q.; Robertson, A. W.; Warner, J. H. In Situ High Temperature Atomic Level Studies of Large Closed Grain Boundary Loops in Graphene. *ACS Nano* **2016**, *10*, 9165–9173.
- (67) Liu, F.; Wang, M.; Chen, Y.; Gao, J. Thermal Stability of Graphene in Inert Atmosphere at High Temperature. *J. Solid State Chem.* **2019**, 276, 100–103.
- (68) Zhao, Y.; Xu, W.; Li, Q.; Xie, Y.; Schaefer, H. F. Gallium Clusters Gan (n = 1-6): Structures, Thermochemistry, and Electron Affinities. *J. Phys. Chem. A* **2004**, *108*, 7448–7459.
- (69) Gaston, N.; Parker, A. J. On the Bonding of Ga2, Structures of Gan Clusters and the Relation to the Bulk Structure of Gallium. *Chem. Phys. Lett.* **2011**, 501, 375–378.
- (70) Stender, M.; Power, P. P. Reaction of $\{HC(CMeNAr)_2\}Li$ (Ar = 2,6-i-Pr₂C₆H₃) with Indium Monochloride to Yield the In In Bonded Dimer $[\{HC(CMeNAr)_2\}InCl]_2$ and the Hydroxide. *Polyhedron***2002**, 21, 525–529.
- (71) Protchenko, A. V.; Urbano, J.; Abdalla, J. A. B.; Campos, J.; Vidovic, D.; Schwarz, A. D.; Blake, M. P.; Mountford, P.; Jones, C.; Aldridge, S. Electronic Delocalization in Two and Three Dimensions: Differential Aggregation in Indium "Metalloid" Clusters. *Angewandte* **2017**, *56*, 15098–15102.
- (72) Protchenko, A. V.; Dange, D.; Harmer, J. R.; Tang, C. Y.; Schwarz, A. D.; Kelly, M. J.; Phillips, N.; Tirfoin, R.; Birjkumar, K. H.; Jones, C.; et al. Stable GaX2, InX2 and TlX2 Radicals. *Nat Chem.* **2014**, *6*, 315–319.
- (73) Protchenko, A. V.; Dange, D.; Blake, M. P.; Schwarz, A. D.; Jones, C.; Mountford, P.; Aldridge, S. Oxidative Bond Formation and Reductive Bond Cleavage at Main Group Metal Centers: Reactivity of Five-Valence-Electron MX 2 Radicals. *J. Am. Chem. Soc.* **2014**, *136*, 10902.
- (74) Schnepf, A.; Schnöckel, H. Metalloid Aluminum and Gallium Clusters: Element Modifications on the Molecular Scale? *Angew. Chem. Int. Ed.* **2002**, *41*, 3532–3554.
- (75) Humphrey, W.; Dalke, A.; Schulten, K. VMD: Visual Molecular Dynamics. J. Mol. Graph. 1996, 14, 33–38.

(76) Briggs, N.; Bersch, B.; Wang, Y.; Jiang, J.; Koch, R. J.; Nayir, N.; Wang, K.; Kolmer, M.; Ko, W.; La, A. De; Duran, F.; et al. Atomically Thin Half-van Der Waals Metals Enabled by Confinement Heteroepitaxy. *Nat. Mater.* **2020**, *19*, 637.